Metal cutting experiments and modelling for improved determination of chip/tool contact temperature by infrared thermography

Pedro-J. Arrazola (2)[a,*], Patxi Aristimuno [a], Daniel Soler [a], Tom Childs (1)[b]

[a] Faculty of Engineering, Mondragon University, Mondragon 20100, Spain
[b] School of Mechanical Engineering, University of Leeds, LS29JT, UK

ARTICLE INFO

ABSTRACT

Temperature measurement in metal cutting at the chip and work contact is of central importance due to temperature dependence of tool wear and surface integrity. Infrared thermography is commonly employed to determine the tool side face temperature in orthogonal cutting but temperature needs to be estimated at the tool chip contact area. This experimental and modelling study of AISI 4140 steel and Ti6Al4V titanium alloy cut respectively by P and K grade cemented carbide tools at practical cutting speeds and feeds shows the relationship between side face and in-contact temperature, for the more certain use of the infra-red thermography method.

© 2015 CIRP.

1. Introduction

How to measure temperatures in metal cutting at the chip and work contact with the cutting tool continues to receive attention because of the central importance of temperature to the linked problems of tool wear and cut surface integrity [1,2]. One direct method is the tool/work thermocouple technique though it is much criticised for being responsive only to average contact temperature and the uncertainty of its calibration [1]. Another method is infrared thermography. The schematic Fig. 1a shows a camera viewing the side face of a tool used for orthogonal cutting ([3–5], see also [6]). Chip side flow requires that the tool overhangs the work by a width d. A typical value is d = 0.3 mm for uncut chip thickness h = 0.1–0.2 mm. The recorded side face temperature is thus an unknown amount lower than the temperature even at the edge of the contact, let alone lower than that in the contact.
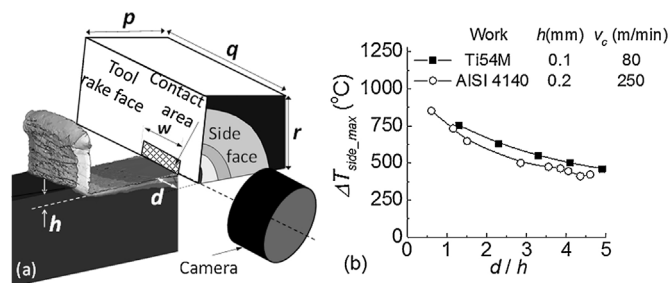
Fig. 1b is a recent result showing ΔT_{side_max}, the maximum side face temperature, reducing the larger is d/h for two typical cases, machining a Ti alloy and a low alloy steel [7]. Measurements also exist for d = 0.3 mm and a range of h and cutting speed v_c. There are published [8–10] comparable measurements by the tool/work thermocouple method. Fig. 2 records results from both methods. Because the h, v_c conditions are not identical, to aid comparison temperatures are partially non-dimensionalised by the specific cutting force F_C^* and h and v_c are combined to the product hv_c.

Fig. 2 shows that for steel the in-contact temperature from the tool/work thermocouple method is significantly higher than the side face temperature from infrared thermography but for Ti alloys the two methods give overlapping results. The hv_c ranges differ between the two groups of alloys due to their different thermal diffusivities.

This paper combines modelling and a modified infrared temperature measurement method to suggest that the difference between the steel and Ti alloy characteristics results from the different tool temperature distributions that occur. The infrared temperature measurement method provides a way directly to view rake face temperatures. Maximum rake face temperature is
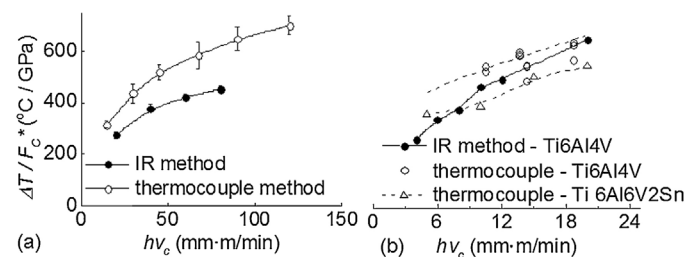

Fig. 1. (a) Schematic view of infrared thermography set up with notation, (b) $\Delta T_{side-max}$ dependence on d/h, machining a Ti alloy and a steel [7].

Fig. 2. Comparisons of rake temperature measurements by tool/work thermocouple and infrared thermography methods for (a) AISI 4140, h = 0.2, 0.3 mm; v_c = 50–400 m/min; (b) Ti alloys, h = 0.1–0.25 mm, v_c = 40–110 m/min.

* Corresponding author.
  E-mail address: pjarrazola@mondragon.edu (P.-J. Arrazola).

measured 120–380 °C higher than at the side face. This is more than predicted in [6] and significant for understanding tool wear.

2. Modelling and simulation strategy and results

The steady state tool temperature distribution when machining with the orthogonal cutting geometry of Fig. 1a is simulated using the commercial software AdvantEdge-3D, to obtain expected side face and rake contact temperatures at different overhangs d.

Two basic issues are addressed. One is that the typical cut time or distance of a simulation is not usually long enough for the steady state to be reached away from the chip/tool contact region. This is overcome here by choosing the tool density ρ and specific heat C to be much lower than in reality (1000 kg/m^3 and 1 J/kg K respectively): the steady state temperature is reached more quickly the lower is ρC; it does not depend on ρC but only on the tool thermal conductivity K_{tool}. The other is that the size of the tool model is much less than in reality. The tool temperature boundary conditions (fixed temperature, adiabatic, or with heat loss) are consequently artificial. This is overcome by simulations with ever increasing tool size (p, q, r dimensions as in Fig. 1a) and with Newton cooling tool surface boundary conditions of varying heat transfer coefficient h_{tc}, until tool contact and overhang temperatures are obtained insensitive to those conditions.

Fig. 3 explains the tool temperature boundary conditions, their effect on the tool temperature distribution, and the criterion for determining a large enough tool. Newton cooling occurs over all tool surfaces (Fig. 3a) except the side face which is adiabatic, to match the condition of dry cutting. As a result the tool heats up until its surfaces are hot enough for the heat flow from the chip to the tool to be dissipated through the surfaces. In the example the tool is small (p, q, r 1.5–2.5 mm) and h_{tc} = 500 W/m^2 K, slightly high for dry cutting. The tool has heated to $\approx$800 °C to achieve the steady state. Fig. 3b shows mid-plane tool temperatures for this case. As tool size is increased, the far-regions of the tool become cooler and the temperatures as in Fig. 3b change. A large enough tool is one for which the change becomes negligible. The closer is h_{tc} to a realistic size, the more accurate is the result.
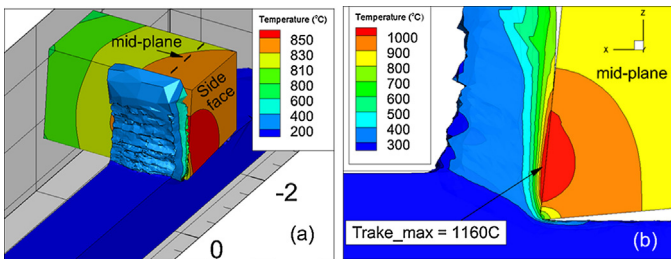
Fig. 3. Example simulation, AISI 4140 cut by P-carbide, h = 0.2 mm, v_c = 250 m/min; w, p, q, r (mm, see Fig. 1) = 1.5, 2.5, 1.5: (a) general view of temperature contours, (b) detail of contact mid-plane section.

2.1. Simulation conditions and outputs

Simulations are performed for AISI 4140 and Ti6Al4V machined by P- and K-carbide tools. Eq. (1) is the flow stress for AISI 4140 up to 900 °C. Above that, flow stress reduces linearly to zero at the AISI 4140's melting point. Eq. (1) is validated experimentally in [8]. Eq. (2) for Ti6Al4V combines a flow stress law (2a) with a plastic failure strain law (2b). It leads to saw-tooth chips though it is not claimed that it does so in a physically realistic manner.

$$\bar{\sigma}\,(\text{MPa}) = 990\left(1 + \frac{\bar{\varepsilon}}{0.0094}\right)^{0.029}(1 + \dot{\bar{\varepsilon}})^{0.022}(1 - 6.7.10^{-4}T + 3.7.10^{-7}T^2)$$
(1)

$$\bar{\sigma}\,(\text{MPa}) = 895\left(1 + \frac{\bar{\varepsilon}}{0.076}\right)^{0.19}\left(1 + \frac{\dot{\bar{\varepsilon}}}{0.01}\right)^{0.037}(1 - 6.06.10^{-4}T)$$
(2a)

$$\int_0^{\bar{\varepsilon}_f} \frac{d\bar{\varepsilon}}{0.4\exp[1.5(p/\bar{\sigma})]} = 1.0$$
(2b)

Work thermal conductivity and diffusivity for AISI 4140 are 39 W/m K and 8.7 mm^2/s; and for Ti6Al4V are 6 W/m K and 2.5 mm^2/s. Tool thermal conductivities are 50 W/m K (P-carbide) and 100 W/m K (K-carbide).

Simulations are carried out for h = 0.1, 0.2 mm, v_c = 75, 250 m/min for AISI 4140 and 40, 80 m/min for Ti6Al4V, and for w = 1, 2 mm, to match the conditions of Fig. 2. Tool rake angle γ = 6°. As well as temperature distributions, cutting and thrust forces F_C and F_T are outputs from the simulations.

2.2. Tool size and h_{tc} dependence of tool temperature fields

The simulations' predictions of how tool temperatures stabilise with increasing tool size for different input values of h_{tc} and different machining conditions are summarised in Figs. 4–6.

For machining AISI 4140, with h = 0.1 mm, v_c = 250 m/min (Fig. 4), mid-plane temperature contours do not alter with increasing tool size once a tool size (mm) of (p, q, r) = (5, 4, 5) is reached in the case that h_{tc} = 5000 W/m^2 K (Fig. 4a) but (20, 5, 20) is needed when h_{tc} = 200 W/m^2 K (Fig. 4b). The temperature contours for both these cases are similarly shaped. The main difference between them is that for h_{tc} = 200 W/m^2 K, tool temperatures are 25–50 °C higher than for h_{tc} = 5000 W/m^2 K.

This difference is insignificant compared to changing h and v_c. The stabilised contours for h = 0.2 mm, v_c = 250 m/min, and h = 0.1 mm, v_c = 75 m/min are seen in Fig. 5a and b. As hv_c reduces
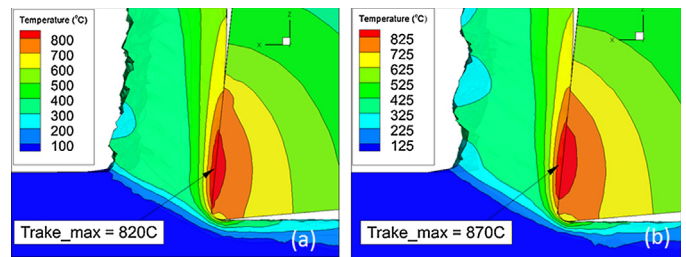
Fig. 4. AISI 4140 cut by P-carbide, h = 0.1 mm, v_c = 250 m/min: h_{tc} (W/m^2 K) and (p, q, r mm) (a) 5000 and (5, 4, 5), (b) 200 and (20, 5, 20).
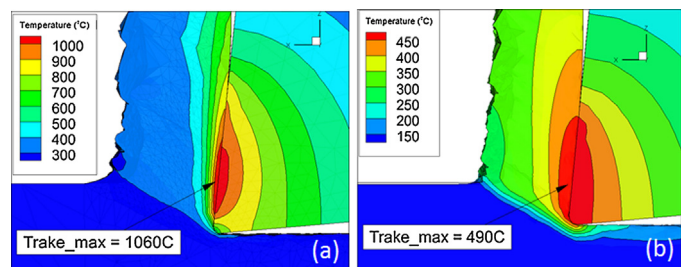
Fig. 5. AISI 4140 cut by P-carbide, h_{tc} (W/m^2 K) and (p, q, r mm) 5000 and, (5, 4, 5): (a) h = 0.2 mm, v_c = 250 m/min; (b) h = 0.1 mm, v_c = 75 m/min.
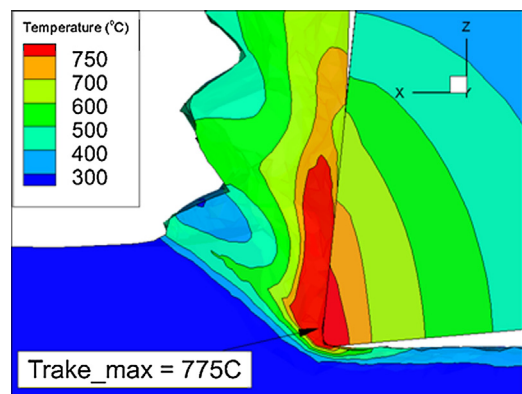
Fig. 6. Ti6Al4V cut by K-carbide: h = 0.2 mm, v_c = 40 m/min, h_{tc} (W/m^2 K) and (p, q, r mm) 5000 and (5, 4, 5).

(Figs. 5a to 4 to 5b), the temperature gradient along the rake face from the cutting edge to the maximum temperature point reduces. The temperature gradient in the tool beneath the chip/tool contact also decreases. (The effect of increased tool size on temperature distribution is directly seen by comparing Figs. 5a and 3b.)

Fig. 6 shows the stabilised temperature contours for Ti6Al4V machined by K-carbide. Maximum contact temperature occurs at the cutting edge.

All these differences are qualitatively as expected from classical heat conduction analyses of temperatures in metal cutting [11]. They validate that the proposed ways of dealing with short cut distance and small tool size are sound.

2.3. Predictions relevant to use of infrared thermography method

Fig. 7 shows an example of tool rake and side face temperature contours. The line AB (Fig. 7a) parallel to the cutting edge passes through the maximum temperature region. Temperature along AB is recorded as a function of fractional distance 0–1.0 across the depth (width) of cut. Maximum side face temperature (Fig. 7b and c) is obtained at varying overhangs d.

Fig. 8 gathers simulation results of AISI 4140 cut by P-carbide and Ti6Al4V cut by K-carbide, over a range of hv_c. Fig. 8a shows in-contact temperature variation along AB for AISI 4140. ΔT, the variation from mid to edge of contact, increases with increasing hv_c. Fig. 8c shows ΔT not increasing for Ti6Al4V. Fig. 8b and d shows for both materials decreasing T_{side_max} with increasing d/h, by 75–125 °C per unit increase in d/h. T_{side_max} extrapolated to $d/h = 0$ links to the edge of contact temperatures in Fig. 8a and c.

These results can explain Figs. 1b and 2. Fig. 1b's reduction of T_{side_max} with d/h is the same as that in Fig. 8b and d. Fig. 2's difference between AISI 4140 and Ti6Al4V is explained by AISI 4140's larger in-contact temperature difference ΔT at high h and v_c (Fig. 8a). This in turn is explained by the peak rake face
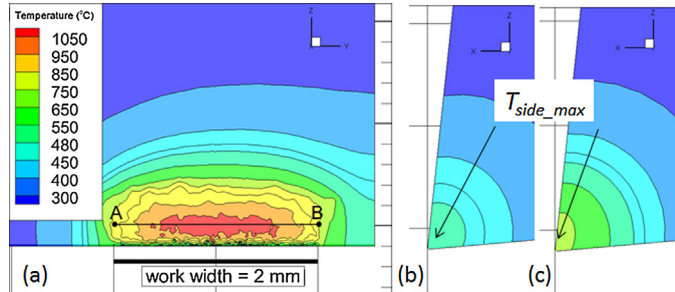

Fig. 7. (a) Rake face temperature contours, AISI 4140 cut by P-carbide, h = 0.2 mm, v_c = 250 m/min, w = 2 mm, d = 0.55 mm; (b, c) side face contours, d = 0.55 mm (b), 0.22 mm (c) (ambient temperature = 20 °C).
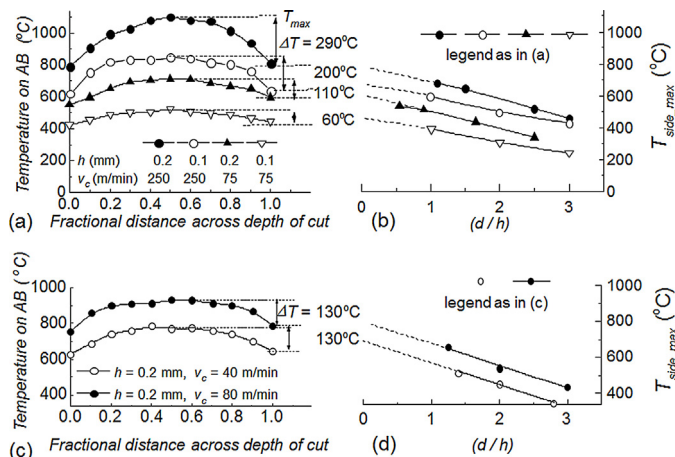

Fig. 8. (a, c) Temperatures along AB for (a) AISI 4140, (c) Ti6Al4V; (b, d) side face temperature variation with d/h for (b) AISI 4140, (c) Ti6Al4V. $(p, q, r$ mm) = (5, 4, 5), h_{tc} = 5000 W/m² K. For Ti6Al4V temperatures are averages over one cycle of saw-tooth formation.

temperature being more localised the higher is hv_c (Figs. 5b to 4a to 5a), and more localised for AISI 4140 than for Ti6Al4V (Fig. 6).

Fig. 8b, d are produced by varying d and extracting T_{side_max} as shown in Fig. 7, to mimic the experimental method behind Fig. 1b. Another experimental approach is directly to observe the tool rake face (see Section 3). Relevant to that, temperatures may be extracted along lines such as AB (Fig. 7), extended to the left of A and to the right of B. The predictions from such extractions for AISI 4140 and Ti6Al4V cut at the same v_c and h as in Fig. 8 and with d/h = 3, as well as specific force predictions, are in Section 3.2 where they are compared with experimental results (Figs. 11–13). In this case $(p, q, r$ mm) = (20, 5, 20). h_{tc} = 200 W/m² K.

3. Infrared thermography experiments and results

3.1. A modified experimental method

A modified infrared thermography method has been developed to allow the tool rake face, rather than the side face, to be imaged. Fig. 9a (compare with Fig. 1a) schematically shows the changed orientation of the camera relative to the tool. Fig. 9b shows the actual set-up on a CNC vertical milling machine. The tool and tool holder are mounted on a dynamometer (Kistler type 9121). It and the camera (FLIR type Titanium 550M) are fixed to the table of the machine. The work, in the form of tube, is held in and rotated by the machine spindle. Machining proceeds with vertical spindle feed, as described in [5].
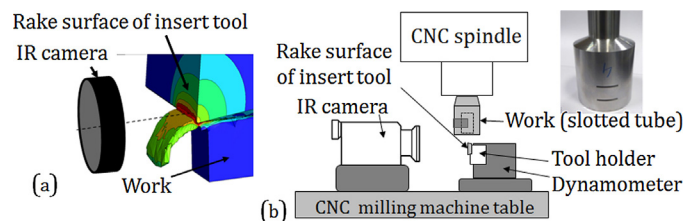

Fig. 9. Schematics of the experimental set-up.

The tube, 50 mm diameter, wall thickness 1 mm, shown inset in Fig. 9b, is machined from solid bar, leaving a solid base at one end for holding in the spindle. A circumferential slot of ≈45° extent is cut in the tube. Machining proceeds for 2–5 s to allow a steady state temperature to be developed before the slot is reached. Then interruption to the cut reveals the rake face to the camera. The time to reach a steady state is found from initial tests imaging the overhang region in continuous cutting. The frame rate is 832 Hz. This allows 3–5 images to be recorded per slot passage. Integration time is 200 μs.

Cutting is performed dry, as required by the thermography. The camera views the tool through a slit in a metal cover (not shown) that surrounds the cutting region. This avoids hot chips degrading the thermography.

Results are reported for AISI 4140 (290 ± 10 HB) and Ti6Al4V (250 ± 15 HB), respectively cut with uncoated plane rake face P10 and K10 carbide tools, γ = 5°, edge radius 5 μm, and v_c, h as in Fig. 8.

Each test is carried out with a new tool. Rake face images are recorded at a wavelength λ = 4 μm (the camera, with an InSb detector array, is used with a narrow bandwidth filter). Radiation temperature RT (K) is converted to true temperature T (K) by Eq. (3), based on Planck's law. ε is the tool surface emissivity and c = 14,389 μm K. Previous measurement with the same batch of P-carbide tools, including surface finish, has given ε = 0.4 ± 0.1 [3].

$$\frac{1}{T} (K) = \frac{1}{RT} (K) + \lambda \ln\left(\frac{\varepsilon}{c}\right) \tag{3}$$

3.2. Experimental results

Not every test gives an observable rake face at cut exit: chips may adhere to the rake face, particularly for Ti6Al4V. Commonly,
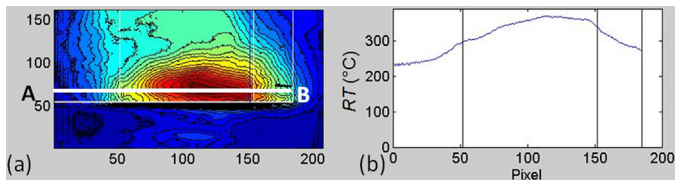
Fig. 10. (a) Infrared rake face image, (b) radiation temperature along AB; AISI 4140 cut by P-carbide, v_c = 75 m/min, h, w, d = 0.1, 1, 0.3 mm.

only 1 in 2 to 1 in 4 tests give useable results. Fig. 10 is one such: in (a) the thin white line traces the tool rake face boundary. The thick white line is that from which the temperature profile in (b) is obtained. The units of distance are pixels: 1 pixel = 10 μm.

Figs. 11 and 12 compare predicted rake face temperature profiles from Section 2.3 with experimental values along AB (Fig. 10), for AISI 4140 and Ti6Al4V and w = 1 mm, d = 3 h. The regions marked side flow are those over which simulated chip thickness reduces from its central value and chips spread to a greater width than w. Fig. 13 compares predicted and experimental specific forces. In Fig. 13, simulated specific forces equal experimental ones for AISI 4140 but are 25% lager for Ti6Al4V. For this reason in Fig. 12 (for Ti6Al4V) temperatures are compared on a basis of T/F_C^*.
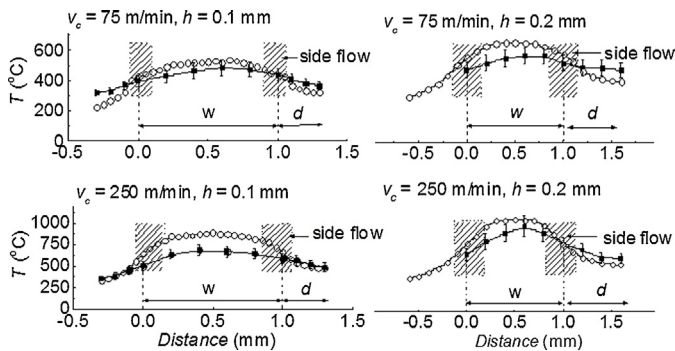

Fig. 11. Simulation (○) and experimental (□) temperature profiles parallel to cutting edge for AISI 4140. In each row the ordinate scale in the right column is the same as that in the left column.
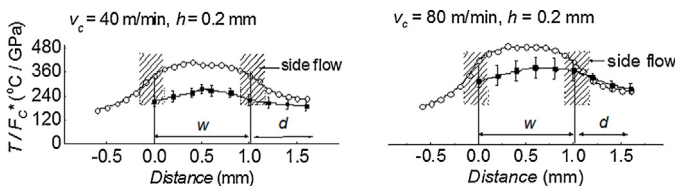

Fig. 12. Profiles parallel to cutting edge of T/F_C^* for Ti6Al4V, other details as in Fig. 11.
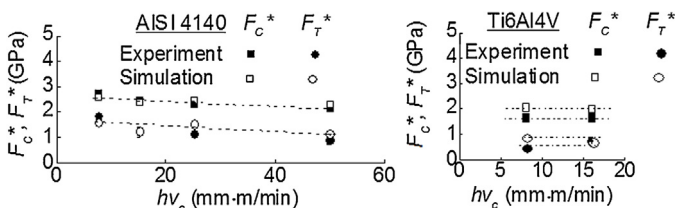

Fig. 13. Experimental and simulated specific forces.

4. Discussion

The experiments show that tool side face temperature is less than the maximum contact temperature by an amount increasing from 120 to 380 °C for AISI 4140 when d/h = 3 and as v_c and h are increased from 75 to 250 m/min and 0.1 to 0.2 mm. For Ti6Al4V the amounts are 130 and 170 °C for v_c = 40 and 80 m/min.

The trend is similar to but less than predicted by simulations. It supports Section 2.3's explanation of the differences in Fig. 2

between the AISI 4140 and Ti6Al4V infrared and thermocouple measured temperatures, namely that the peak rake temperature is more localised for AISI 4140 than for Ti6Al4V, the more so the larger is hv_c, as expected from heat conduction theory [11].

Figs. 11 and 12 show maximum experimental temperatures less than simulations by 5–25%, except for Ti6Al4V at 40 m/min which is anomalous. Estimated uncertainty in temperature measurement is expected to be ±10% at 500 °C [3]. Adhesion of work material on the rake face, with consequent systematic uncertainty in ε there, may account for the remainder. The error bars in Figs. 11 and 12 are from the uncertainty ±0.1 imposed on ε (Section 3.1) to allow for this but a lower ε in than out of the contact would bring experiments and simulations closer together.

Figs. 11 and 12 also show the simulated differences between maximum and side face temperatures are 1.4–2.7 times greater than from experiments. Emissivity uncertainty may contribute to this but it is believed that there is too large a simulated temperature variation in the chip side flow regions, arising from the chip/tool friction law $\tau = \min \bar{\sigma}/\sqrt{3}, \mu\sigma_n$ with τ, μ and σ_n having usual definitions. This law does not properly reflect the contact conditions in the plastic secondary shear zone as discussed in [12]. It can give rise to a deficit in friction work as σ_n reduces towards the contact edge.

5. Conclusions

Infrared thermography of tool rake faces shows maximum chip/tool contact temperatures to be 120–380 °C higher than tool side face temperatures measured in previous work on machining AISI 4140 and Ti6Al4V alloys in practical conditions. Simulations explain the observed trends although the simulations are not perfect, overestimating rake face temperature gradients in the chip side flow regions, possibly due to the applied friction law.

Acknowledgements

References

[1] Davies MA, Ueda T, M'Saoubi R, Mullany B, Cooke AL (2007) On the Measurement of Temperature in Material Removal Processes. *Annals of the CIRP* 56(2):581–604.

[2] Jawahir IS, Brinksmeier E, M'Saoubi R, Aspinwall DK, Outeiro JC, Meyer D, Umbrello D, Jayal AD (2011) Surface Integrity in Material Removal Processes: Recent Advances. *Annals of the CIRP* 60(2):603–626.

[3] Arrazola PJ, Arriola A, Davies MA, Cooke AL, Dutterer BS (2008) The Effect of Machinability on Thermal Fields in Orthogonal Cutting AISI 4140 Steel. *Annals of the CIRP* 57(1):65–68.

[4] Arrazola PJ, Arriola I, Davies MA (2009) Analysis of Influence of Tool Type, Coatings and Machinability on the Thermal Fields in Orthogonal Machining of AISI 4140 Steels. *Annals of the CIRP* 58(1):85–88.

[5] Armendia M, Garay A, Villar A, Davies MA, Arrazola PJ (2010) High Bandwidth Temperature Measurement in Interrupted Cutting of Difficult to Machine Materials. *Annals of the CIRP* 59(1):97–100.

[6] M'Saoubi R, Chandrasekeran H (2004) Investigation of the Effects of Tool Micro-Geometry and Coating on Tool Temperature During Orthogonal Turning of Quenched and Tempered Steel. *International Journal of Machine Tools and Manufacture* 44:213–224.

[7] Soler D, Childs THC, Arrazola PJ (2015) A Note on Interpreting Tool Temperature Measurements from Thermography. *Machining Science and Technology* 19:174–181.

[8] Childs THC, Otieno AW (2012) Simulations and Experiments on Machining Carbon and Low Alloy Steels at Rake Face Temperatures up to 1200°C. *Machining Science and Technology* 16:96–110.

[9] Hoyne AC, Kapoor SG, Nath C (2013) *Cutting Temperature Measurement During Titanium Machining with an Atomization-Based Cutting Fluid (ACF) Spray System*. *ASME Paper IMEC2013-63898*.

[10] Kitagawa T, Kubo A, Maekawa K (1997) Temperature and Wear of Cutting Tools in High Speed Machining of Inconel 718 and Ti–6Al–6V–2Sn. *Wear* 202:142–148.

[11] Childs THC, Maekawa K, Obikawa T, Yamane Y (2000) *Metal Machining: Theory and Applications*, Arnold, London3. (Chapter 2).

[12] Childs THC (2006) Friction Modelling in Metal Cutting. *Wear* 260:310–318.